Journal of Photochemistry and Photobiology A: Chemistry 148 (2002) 315–322

Journal of Photochemistry and Photobiology A:Chemistry

www.elsevier.com/locate/jphotochem

# Synthesis of size-controlled silica-supported $TiO_2$ photocatalysts

R. van Grieken* , J. Aguado, M.J. López-Muñoz, J. Marugán

*ESCET, Universidad Rey Juan Carlos, C/Tulipán s/n, 28933 Móstoles, Madrid, Spain*

Received 24 July 2001

**Abstract**

Supported nanocrystalline titanium dioxide has been prepared by a sol–gel method through the use of mesoporous silica materials. The work has been addressed to study the effect of the different type of silica support on the mean titania particle size and their effect in the photocatalytic activity. The prepared samples have been characterised by powder X-ray diffraction (XRD), nitrogen adsorption, UV–VIS spectroscopy, EDS, and TEM and their photocatalytic activity has been checked for cyanide oxidation in liquid phase. A correlation between the textural properties of the chosen silica support and the diameter of the obtained titania particles is observed. The use of mesostructured SBA-15 silica support with a pore diameter around 7 nm has shown to be an effective method to obtain photocatalysts with controlled $TiO_2$ particle size even at high semiconductor contents (up to 60 wt.%). 

*Keywords:* Nanocrystalline titanium dioxide; Photocatalysis; Mesostructured silica; Controlled particle size

## 1. Introduction

Heterogeneous photocatalysis has shown a high potential in applications related to liquid phase pollution control processes [1,2]. Among the metal oxides semiconductors suitable for photocatalytic processes, titanium dioxide is the most widely used due to both its high photocatalytic activity and its chemical/photocorrosion stability in the reaction conditions. The efficiency of some commercial $TiO_2$ in photooxidation processes has been fully proved; however, most of those samples usually have small particle sizes so that the problems arising in the catalyst-recovering stage hinder their effective commercial application. On this basis, a great effort has been focused in developing supported titania catalysts offering high active surface area, together to better recovery properties. Up-to-date most of the reported works are mainly based on sol–gel processing using an inert amorphous matrix such as $SiO_2$ [3,4]. Although this method achieves improved recovery of the catalyst particles, it usually does not allow controlling the particle size. The latter is an important parameter in the titania photocatalytic efficiency as the predominant way of the recombination of electron–hole pairs may be different depending on the semiconductor particle size range [5]. It is well known that in the nanometer size range, the physical and chemical properties of the semiconductors are modified as compared with bulk semiconductor and strongly affected by the particle size. Small variations in the particle diameters involve great modifications in the surface/bulk ratio thus modifying the significance of volume and surface $e^-/h^+$ recombination. Therefore, control of the particle size in nanocrystalline titania catalysts becomes crucial.

A suitable synthesis method for obtaining $TiO_2$ having defined particle size could be the use of a structured silica support with a suitable mean pore size that would induce controlled oxide particle growth. To accomplish this objective, mesostructured silica such as MCM-41 and SBA-15 appear to be the most appropriate supports due to their properties of high surface areas, ordered frameworks and narrow pore size distributions. Previous works have been reported on the use of MCM-41 as support for titania coating. Langford and Langford [6] supported titania particles whose size was defined not by the support but by the precursor sol synthesis conditions. Aronson et al. [7] developed a technique for grafting titania on MCM-41 and FSM-16 samples, obtaining $TiO_2$ nanoclusters ($n \sim 30$–70 $TiO_2$/cluster) without pore clogging. Such small sizes, however, may not be adequate for photocatalytic purposes as detrimental quantum effects may appear counteracting the advantages of such high titania surface area [8].

In the present work we have investigated the synthesis of size-controlled nanocrystalline $TiO_2$ supported on mesostructured silica materials such as MCM-41 and SBA-15 using the sol–gel technique. Titania particles in the size range of 6–10 nm without significant pore clogging of the mesostructured channels have been obtained by constraining the particle growth into the support. The limitation of the $TiO_2$ particle growth induced by the SBA-15

* Corresponding author. Tel.: +34-91-4887007; fax: +34-91-6647490.
*E-mail address:* r.vangrieken@escet.urjc.es (R. van Grieken).

1010-6030/02/$ – see front matter 
PII: S1010-6030(02)00058-8

silica support is specially remarkable as the titania content increases in the catalysts. Photocatalytic activity of the samples has been tested in terms of cyanide oxidation in liquid phase.

## 2. Experimental

### 2.1. Synthesis

Nanocrystalline titanium dioxide was prepared via sol–gel hydrolysis and condensation of an isopropanol solution of titanium tetraisopropoxide ($Ti(OC_3H_7)_4$, Alfa Chemicals) (TTIP) in the presence of the selected silica support. Different supports were used: a commercially available non-structured $SiO_2$ (Grace Sylopol 2104) and mesostructured silica materials (MCM-41 and SBA-15) prepared in our laboratory.

MCM-41, a uniform mesoporous material [9], was synthesised at room temperature following a two-step sol–gel process based on a method recently reported for Al-MCM-41 [10], using as precursors hexadecyltrimethylammonium chloride (25 wt.% aqueous solution of $C_{16}H_{33}(CH_3)_3NCl$, Aldrich) and tetraethylorthosilicate ($Si(OC_2H_5)_4$, 99 wt.%, Alfa Chemicals) (TEOS). The product was dried at 110 °C and calcined at 550 °C. The synthesis of SBA-15, was performed according to the method reported by Zhao et al. [11] by reacting a solution of Pluronic 123 (Aldrich) in HCl with TEOS, followed by calcination at 550 °C. The resulting solid showed the characteristic well-ordered hexagonal mesoporous silica structure whose pore size was varied by using trimethylbenzene (TMB, Aldrich) as additional chemical reagent in the synthesis [11]. This material will be referred to as SBA-15/TMB.

To obtain the supported $TiO_2/SiO_2$ materials, a solution with the required amount of TTIP in isopropanol (TTIP:*i*-PrOH weight ratio 1:8) to get 20, 40 and 60 wt.% $TiO_2$ loading was added to each silica support. After stirring the mixture for 45 min at room temperature, water was added until a molar ratio 160 $H_2O$:TTIP was reached. The stirring was then continued for other 45 min. The mixture was centrifuged and the recovered solid was dried at 110 °C overnight and calcined at 550 °C for crystallisation.

Throughout the subsequent discussion, the samples will be named by indicating in the first place the titania content and next the support code: wt.% $TiO_2$_support, e.g. 60% $TiO_2$_SBA-15.

As reference, a 100% $TiO_2$ material was prepared following the procedure described above without addition of any silica support.

### 2.2. Characterisation

X-ray diffraction (XRD) patterns of the samples were recorded on a Philips X'PERT MPD diffractometer using Cu Kα radiation and a step size of 0.02° in the range 20–70°. The step time was 2 s, adequate to obtain a good signal-to-noise ratio in the main reflections of the two studied $TiO_2$ crystalline phases, (1 0 1) anatase ($2\theta \sim 25.3°$) and (1 1 0) rutile ($2\theta \sim 27.4°$). Calcite (1 0 4) peak ($2\theta \sim 29.4°$) was used as internal standard to calculate the instrumental width.

Nitrogen adsorption–desorption isotherms at 77 K were determined in a Micromeritics Tristar 3000 sorptometer. The surface area measurements were carried out according to the Brunauer–Emmett–Teller (BET) method. The pore size distributions were calculated with the DFT Plus software (Micromeritics), applying the Barrett–Joyner–Halenda (BJH) model with cylindrical geometry of the pores.

UV–VIS spectral data were taken in a Varian Cary 500 Scan UV–VIS–NIR spectrophotometer provided with an integrating diffuse reflectance accessory. The spectra recorded in the range 200–500 nm in terms of $F(R)$, the Kubelka–Munk function, were used to calculate the bandgap of the $TiO_2$ materials.

Transmission electron microscopy (TEM) images were taken on a JEOL JEM-2000 FX instrument, working at 200 kV. Prior to the analysis the samples were dispersed in acetone, stirred in an ultrasonic bath and placed on a carbon-coated copper grid. X-ray energy dispersive spectra and elemental mapping were obtained using an EDAX spectrometer attached to SEM (JEOL JSM-6400) working at 20 kV.

### 2.3. Photocatalytic reactions procedure

The photocatalytic runs were performed in a Pyrex batch reactor with cylindrical shape and 1 l as effective sample volume. The UV-source was a 150 W medium pressure Hg lamp (Heraeus TQ-150) immersed within the reactor in a double wall jacket in which water was circulated to prevent overheating of the reaction mixture. Prior to the start of each photocatalytic reaction, the lamp was switched on for 15 min out of the reactor in order to stabilise the emitted radiation power. Concurrently, the suspension made up of the catalyst and the aqueous cyanide solution was saturated with oxygen by continuous air bubbling. The aeration was lasted during the run. The reactions were carried out at 25 °C with a catalyst concentration of 0.5 g/l of $TiO_2$ and 100 ppm as initial concentration of $CN^-$. Aqueous cyanide solutions were prepared with KCN (Scharlab, reagent grade); the initial pH of the reaction solution was adjusted to 12 by addition of NaOH (Scharlab, reagent grade).

Aliquots collected during the photoreaction were filtered through 0.22 μm nylon membranes and analysed for total cyanide concentration with a selective $CN^-$ electrode (Orion 720A). Cyanide concentrations lesser than 5 ppm were determined spectrophotometrically using a pyridine–barbituric acid reagent [12]. Identification and quantification of cyanate and nitrate, the products detected in the cyanide photooxidation runs, were performed by means of ionic chromatography (Metrohm Separation center 733, IC detector 732 and Pump Unit 752), using aqueous solutions of $NaHCO_3$ (2 mM) and $Na_2CO_3$ (1.3 mM) as eluent.

## 3. Results and discussion

### 3.1. Textural properties and characterisation

Fig. 1 displays the nitrogen adsorption–desorption isotherms of the different silica supports. As it can be observed, all the materials exhibit type IV nitrogen isotherms with desorption hysteresis loops types H1 in the case of the SBA-15 and SBA-15/TMB materials and H2 in the commercial silica, indicative of their mesoporosity. The pore size distributions for the supports are also shown in Fig. 1. It is noticeable the wide pore size distribution offered by the commercial silica matrix in contrast with the narrower pore size range showed by the synthesised SBA-15 and SBA-15/TMB materials. Although the pore size distribution of the MCM-41 sample is wider than that obtained for a material synthesised by hydrothermal treatment [9] (Fig. 1), for the purposes of this work it shows suitable properties to be used as support.

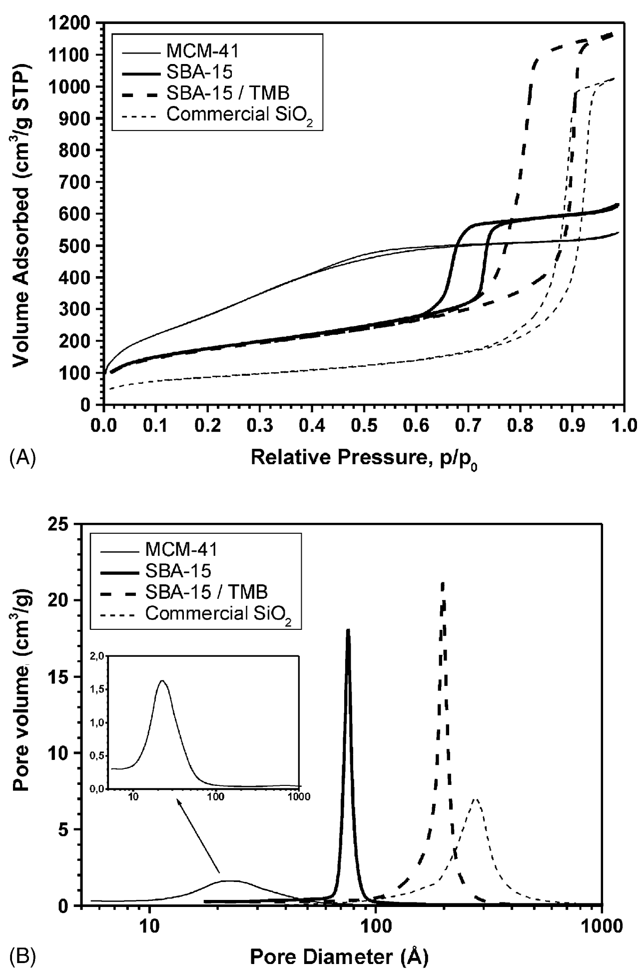


Fig. 1. (A) Nitrogen adsorption–desorption isotherms and (B) pore size distributions of MCM-41, SBA-15, SBA-15/TMB and commercial silica supports.

Table 1 shows the textural properties of the silica supports and the titania loaded samples: $S_{BET}$, specific surface area; $V_P$, pore volume, and pore size corresponding to the maxima of the plotted pore size distributions. Supports within a range of 2–25 nm of pore size were tested in order to study the influence of the silica pore size in the growth of the titania particles. The mesoporous ordered material MCM-41, which presented the higher BET surface area, had a mean pore size of 2.3 nm. The average pore size of 7.5 nm of the hexagonal mesoporous silica structure SBA-15, was modified by the addition of trimethylbenzene in the synthesis, as it has been explained above. The resulting material, SBA-15/TMB, presented a pore size value of 20.0 nm, whereas the BET surface area was slightly lower than the presented by the unmodified SBA-15 silica. Finally, it can be observed that the non-structured commercial silica offered the highest pore size value (27.5 nm) and the smaller surface BET area.

Titania loading on the silica matrix decreases the surface area of the supports as expected for the $TiO_2$ incorporation (Table 1). Such surface reduction is however so drastic in the MCM-41 sample, that it suggests a significant alteration of the support arrangement. On the other hand, it is observed in all the other supports a systematic decrease in their pore volume values, as the titania content increases. This pore volume reduction would indicate that most of the semiconductor particles loading takes place within the ordered channels of the support.

Fig. 2 shows the nitrogen adsorption–desorption isotherms and the pore size distributions of the 20, 40, 60% $TiO_2$_SBA-15 and 20% $TiO_2$_MCM-41 materials, compared with the unloaded supports. The isotherms of the SBA-15-based samples kept the features of the isotherm exhibited by the unloaded support; therefore it is concluded that the mesostructure is maintained upon $TiO_2$ addition. Moreover, it is interesting to note that the calculated pore size distribution (Fig. 2C) is slightly modified even for the sample with the highest titania loading, suggesting a porous structure similar to that present in the unloaded support. Similar results were obtained in the case of the SBA-15/TMB-based samples. By contrast, it can be observed in the 20% $TiO_2$_MCM-41 sample how the titania loading significantly changes the isotherm shape of the support, which is indicative of structure modifications. In addition, the shift of the pore size distribution maximum to much higher values and the wider pore size distribution (Fig. 2D) indicates the breakdown of the structured pore arrangement.

The maintenance of the support framework order upon increasing the Ti/Si ratio was studied by the analysis of the low angle range XRD patterns. Fig. 3 shows the disappearance of the low angle reflection peak observed in the 20% $TiO_2$_MCM-41 sample as compared with the unloaded support. Consequently, it can be inferred the breakdown of the long-range order of the support upon $TiO_2$ addition

Table 1
Textural properties of supports and prepared samples

| | Specific surface area ($m^2/g$) | Pore volume ($cm^3/g$) | Maximum of the pore size distribution (nm) |
|---|---|---|---|
| MCM-41 $SiO_2$ | 1051 | 0.83 | 2.3 |
| SBA-15 $SiO_2$ | 640 | 0.96 | 7.5 |
| SBA-15/TMB | 601 | 1.62 | 20.0 |
| Commercial $SiO_2$ | 317 | 1.59 | 27.5 |
| 100% $TiO_2$ reference | 9 | – | – |
| 20% $TiO_2$ MCM-41 | 294 | 0.57 | 16.0 |
| 20% $TiO_2$ SBA-15 | 532 | 0.78 | 7.0 |
| 40% $TiO_2$ SBA-15 | 442 | 0.69 | 6.5 |
| 60% $TiO_2$ SBA-15 | 349 | 0.60 | 6.5 |
| 20% $TiO_2$ SBA-15/TMB | 517 | 1.40 | 18.5 |
| 40% $TiO_2$ SBA-15/TMB | 414 | 1.08 | 18.5 |
| 60% $TiO_2$ SBA-15/TMB | 304 | 0.78 | 18.5 |
| 20% $TiO_2$ commercial | 299 | 1.16 | 22.5 |
| 40% $TiO_2$ commercial | 246 | 0.94 | 25.0 |
| 60% $TiO_2$ commercial | 179 | 0.67 | 26.0 |

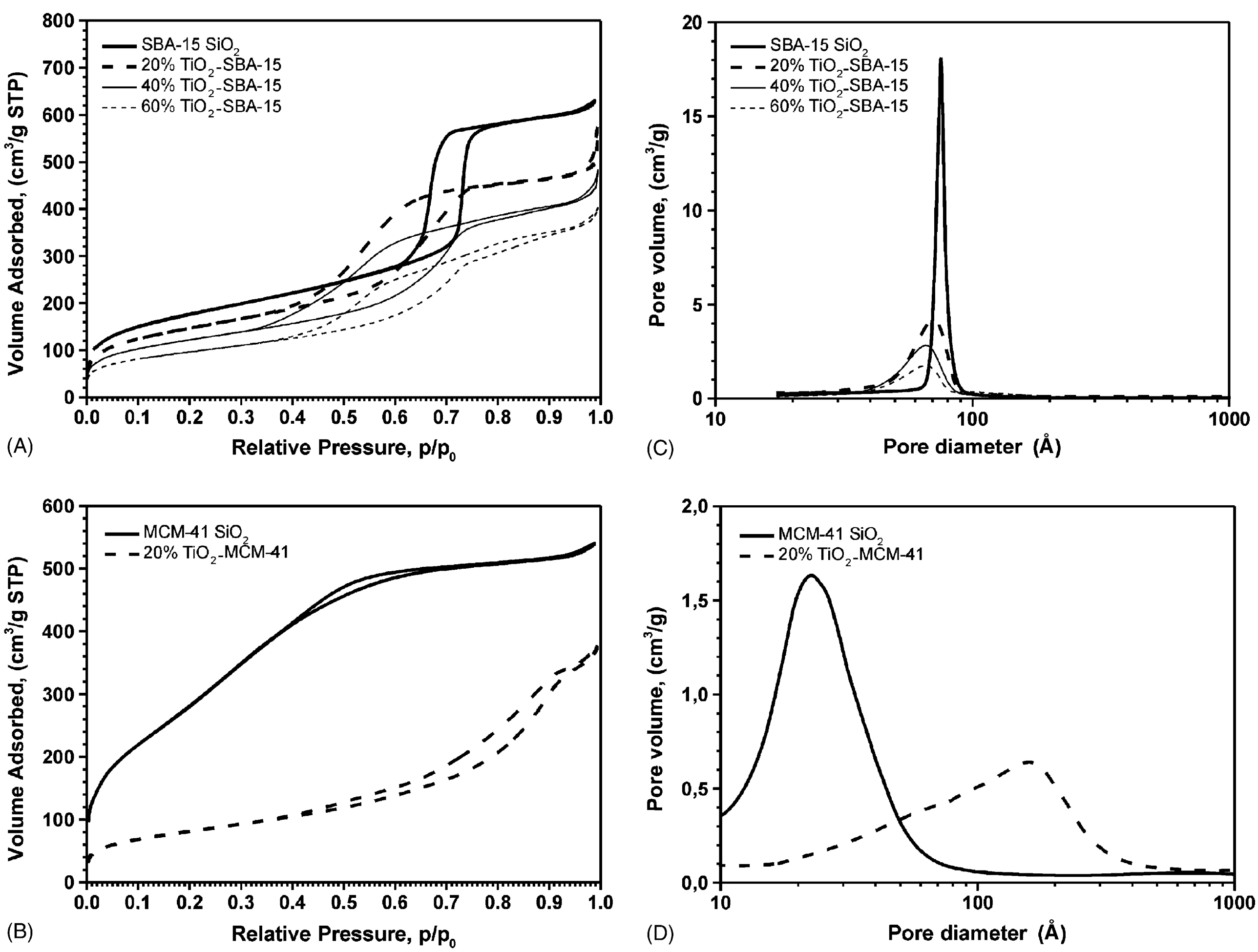


Fig. 2. Nitrogen adsorption isotherms of (A) 20–60% $TiO_2$_SBA-15 and (B) 20% $TiO_2$_MCM-41 samples. Pore size distributions of (C) 20–60% $TiO_2$_SBA-15 and (D) 20% $TiO_2$_MCM-41 samples.

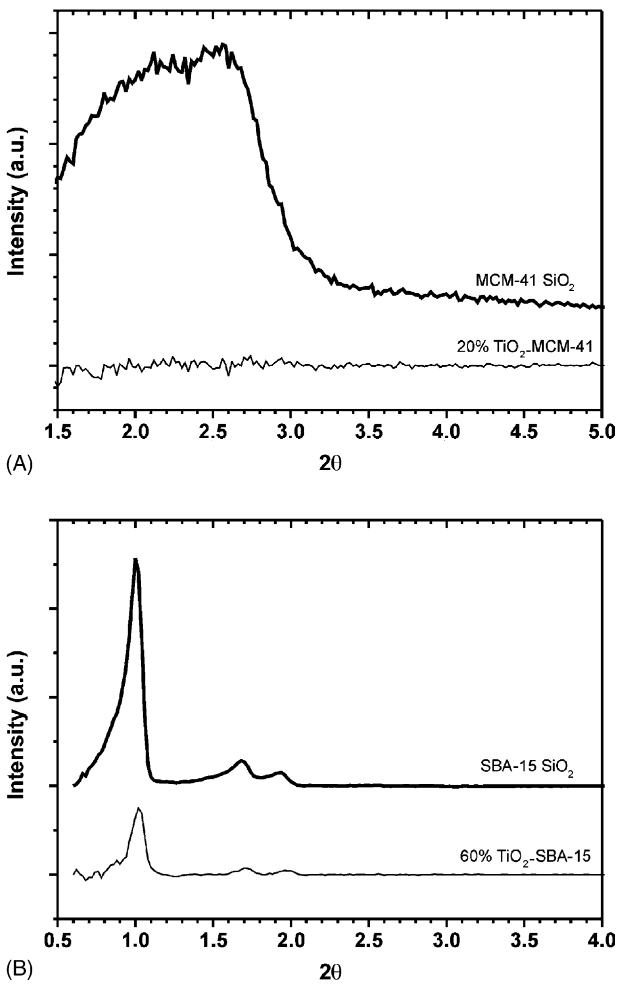


Fig. 3. XRD patterns at low angle of (A) MCM-41 and 20% $TiO_2$_MCM-41 samples and (B) SBA-15 and 60% $TiO_2$_SBA-15 samples.

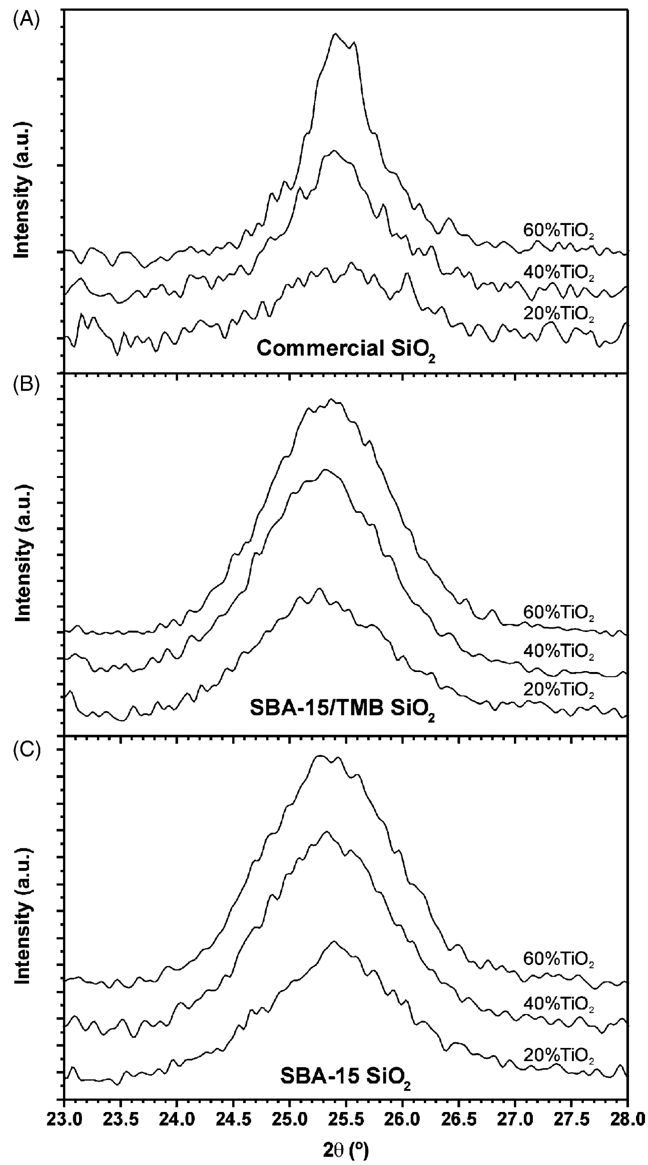


Fig. 4. XRD patterns of $TiO_2$ supported on (A) commercial silica, (B) SBA-15/TMB and (C) SBA-15 silica. Increasing titania loadings in the range 20–60 wt.% are shown for each support.

and calcination, thus explaining the drastic decrease of the surface area mentioned above. In contrast, low angle peaks were detected in the XRD patterns of the SBA-15 and 60% $TiO_2$_SBA-15 samples even at high titania contents (Fig. 3B), thus indicating that the titania particles incorporated to the silica framework prevents the collapse of the silica mesostructure. This assumption was also confirmed by TEM, as it will be shown below.

The XRD patterns at higher angles of the supported $TiO_2$ samples evidenced that anatase was the only titania crystalline phase present in all prepared materials, as indicated by the peak emerging at $2\theta \sim 25.3^\circ$ associated with (1 0 1) anatase diffraction (shown in Fig. 4). No rutile phase was detected in any case according to the absence of the (1 1 0) rutile reflection at $2\theta \sim 27.4^\circ$. By contrast, the 100% $TiO_2$ reference material showed two crystalline phases, anatase and rutile, with a higher proportion of the latter (64%). The average crystallite sizes $\phi_{XRD}$, listed in Table 2, were determined from the Scherrer's equation using the broadening of the (1 0 1) anatase peak reflection with the usual assumption of spherical crystallites. It can be observed the much higher particle size presented by the 100% $TiO_2$ reference material as compared with the supported materials. This may be explained in terms of the formation of big $TiO_2$ agglomerates whose development seems to be limited in the presence of the silica support. It has been previously suggested that a critical size in the range of 40–50 nm must be achieved for the phase transition from anatase to rutile in titania particles [13]. On this basis, the 100% $TiO_2$ reference material would accomplish that required size and so, some rutile formation is induced upon calcination. By contrast, the particle size of the supported titania samples must stabilised them as anatase against phase transition following identical thermal treatment.

The bandgap values of $TiO_2$-supported samples were evaluated from their diffuse reflectance data by plotting the

Table 2
$TiO_2$ particle size of the prepared samples

| | XRD anatase size (nm) | Optical bandgap (eV) | UV–VIS anatase size (nm) |
|---|---|---|---|
| 100% $TiO_2$ reference | 74.0 (rutile > 1 μm) | – | – |
| 20% $TiO_2$ MCM-41 | 8.2 | 3.70 | 7.4 |
| 20% $TiO_2$ SBA-15 | 6.2 | 3.83 | 5.8 |
| 40% $TiO_2$ SBA-15 | 6.7 | 3.74 | 6.8 |
| 60% $TiO_2$ SBA-15 | 6.8 | 3.71 | 7.3 |
| 20% $TiO_2$ SBA-15/TMB | 6.4 | 3.79 | 6.2 |
| 40% $TiO_2$ SBA-15/TMB | 8.1 | 3.63 | 8.7 |
| 60% $TiO_2$ SBA-15/TMB | 9.7 | 3.59 | 9.7 |
| 20% $TiO_2$ commercial | 6.8 | 3.70 | 7.4 |
| 40% $TiO_2$ commercial | 8.0 | 3.66 | 8.1 |
| 60% $TiO_2$ commercial | 12.2 | 3.60 | 9.4 |

square of the Kubelka–Munk function, $F(R)^2$ versus energy (eV). The optical bandgaps (eV) were obtained by extrapolating to zero the linear region of the transformed DR UV–VIS spectra (Table 2). As compared with pure bulk anatase (bandgap value of 3.2 eV [14]) a blue shift of the bandgap absorption edge was observed in all supported samples, which may be explained in terms of the quantum size effects that emerge in semiconductors at small particle sizes [15]. The magnitude of the detected blue shift diminishes as the titania loading increases.

This shift can be used to evaluate $TiO_2$ size for particles near quantum size (∼10 nm), as it has been previously reported [8]. For this reason the method is not valid for estimating the average particle size of the 100% $TiO_2$ sample. Applying the hyperbolic band model, measured bandgap can be related to particle size as follows [15]:

$$\Delta E = (E_g^2 + 4\lambda)^{1/2} = \left( E_g^2 + 2\hbar E_g \frac{(\pi/R)^2}{m^*} \right)^{1/2}$$

where $\Delta E$ is the experimental bandgap, $E_g$ the bandgap of the bulk phase, $R$ the radius of the $TiO_2$ particle and $m^*$ is the reduced effective mass of electron–hole pairs. Assuming a bandgap of 3.2 eV for anatase bulk phase and $m^* = 1.2m_e$ [16], particle sizes were estimated as shown in Table 2. A good correlation is found between the average particle sizes obtained by this method and those ones calculated from the XRD data.

The influence of the silica support on the $TiO_2$ distribution was studied by X-ray energy dispersive analysis performed on a SEM. It was confirmed the nominal Si:Ti ratio in all the samples. The main differences detected in the EDS elemental maps are related to the titania distribution throughout the silica. Whereas a homogeneous dispersion of the titania all over the support is found in the SBA-15-based samples, $TiO_2$ aggregations heterogeneously localised at certain regions are formed on the commercial non-structured silica.

The analysis of the described experimental results shows that for low titania contents (20 wt.%) the dispersion effect induced by the silica supports limits the resulting particle size independently of the available pore width host. Similar average sizes are obtained for 20% $TiO_2$_SBA-15, 20% $TiO_2$_SBA-15/TMB or 20% $TiO_2$_commercial samples (Table 1) suggesting that there is a minimum particle size for titania supported on silica following the calcination treatment. The use of MCM-41 silica must be discarded as proper support due to the small size of the pores to accommodate such $TiO_2$ critical size that leads to the breakdown of the silica mesostructure. Nevertheless, the dispersion effect promoted by the support prevents in all cases the achievement of the minimum size for the anatase to rutile phase transition [13]. In the case of the commercial and SBA-15/TMB supports, both samples with large pore sizes, the mean $TiO_2$ particle size increases as the titania loading increases, as there is enough room for the particle growing process. On the contrary, it is possible to achieve the restriction of the titania particle growth by employing a mesostructured silica with regular and suitable pore size as support. The increase of the titania loading from 20 to 60% does not lead to significant increase in particle size when SBA-15 is used as support, whereas the same increase in titania loading onto a non-mesostructured silica support leads to significant changes in titania particle size.

Correlation between the regular pore width of the mesostructured SBA-15 support and the resulting particle size of titania grown into them was confirmed by the TEM micrographs. Fig. 5 shows the TEM images of both the SBA-15 mesoporous silica and the 60% $TiO_2$_SBA-15 samples. It can be observed the regular distribution of the cylindrical mesopores in the SBA-15 material and how the ordered mesostructure of this support is kept quite unaffected by the incorporation of the titania into the channels. TEM micrographs also confirmed that most of the semiconductor particles are confined in the inner of the mesoporous silica matrix showing a narrow particle size distribution with no evidence of aggregation between the semiconductor particles.

Although the location of the titania particles inside of the mesostructured silica channels could suggest pore clogging mainly at high titania loading, it can be concluded from the textural properties obtained that most of the titania particles are accessible to the reactants, although diffusion should be

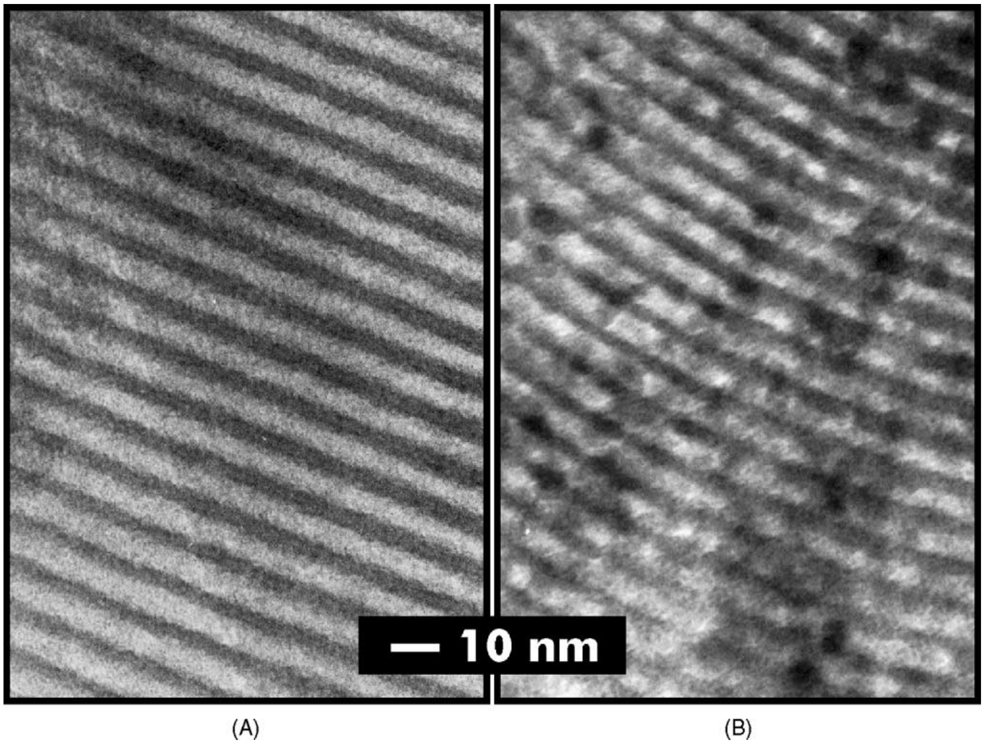


Fig. 5. TEM micrographs of (A) SBA-15 and (B) 60% $TiO_2$_SBA-15 samples.

very restricted in some points of the network. It is interesting to note that according to the similar values between the pore size of the SBA-15 support and the obtained average titania particle size we cannot discard the possible localised clogging effect exercised by some particles. However, pores interconnecting the parallel channels must counteract this effect, as it has been suggested by other authors [20].

### 3.2. Photoactivity for cyanide oxidation

Cyanide photooxidation test reactions were carried out in order to evaluate the activity of the prepared catalysts. Preliminary runs were carried in the absence of catalyst, air and/or radiation. No cyanide photodegradation was observed in these conditions thus showing the studied process is a photocatalytic reaction. In all the performed reaction runs the formation of cyanate as the first product of cyanide photocatalytic oxidation was detected. The mass balance between cyanide disappearance and cyanate formation allowed us to discard any $CN^-$ stripping during the course of the reaction found by some authors [17]. After the complete disappearance of cyanide, nitrate species were detected. The obtained results agree with the mechanism previously proposed for cyanide photooxidation on polycrystalline $TiO_2$ which implies in the first stage the oxidation by photogenerated holes of $CN^-$ to $CNO^-$, the latter further oxidised to nitrate species [18,19].

The photocatalytic activities of $TiO_2$_SBA-15 and $TiO_2$_commercial silica samples are shown in Fig. 6 as cyanide degradation after 2 h. Their respective initial rate constants for cyanide oxidation, normalised to the titania content of the materials are also displayed. It can be observed that there are not significant differences in activity between the samples containing 20 wt.% $TiO_2$ loading in spite of the different surface areas of both catalysts. It should be noted, however, that the crucial parameter in photocatalytic processes should be the UV-irradiated $TiO_2$ surface and similar mean titania particle sizes are obtained for both catalysts (Table 1). Moreover, the analogous experimental activities shown by both samples allows to discard a potential clogging that would be suggested by the one-dimensional straight channel system of the SBA-15 support in contrast to the apparently more accessible pore system of the non-structured silica. By increasing the $TiO_2$ loading it is observed an enhancement of the cyanide photooxidation activity on both supports. Since less catalyst weight is needed to keep the semiconductor concentration constant (0.5 g/l) as $TiO_2$ loading increases, such trend might be explained in terms of scattering effects, which could reduce the effective photonic efficiency. However, whereas the improvement of the catalytic activity with increasing $TiO_2$ loading is moderate in the samples supported on the non-structured silica matrix, it is more pronounced in the case of SBA-15 material, thus suggesting additional reasons to explain the variations of the rate constants. According to Zhang et al. [8] the photocatalytic activity depends on the titania mean particle size with an optimum value around 10 nm, although other authors [21] claimed improved activity for particles

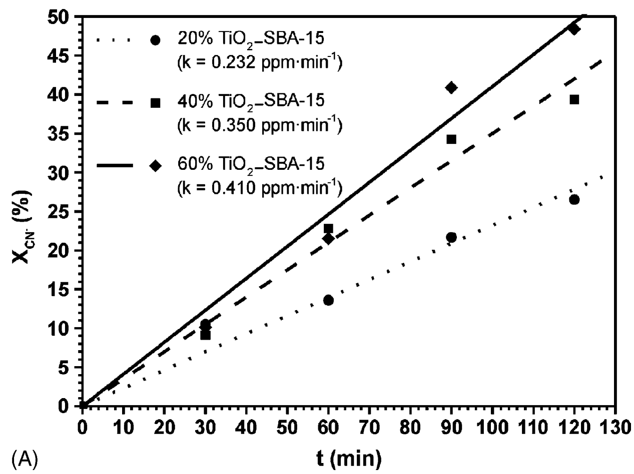


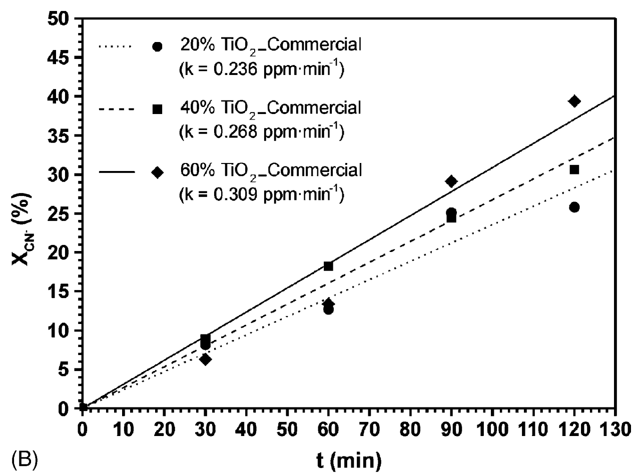


Fig. 6. Kinetics of cyanide photooxidation in the presence of (A) 20–60% $TiO_2$_SBA-15 samples and (B) 20–60% $TiO_2$_commercial $SiO_2$ materials.

below such value. Taking into account that similar scattering effects due to the solid particles are expected for equal titania loading in both supports, the differences in the mean particle sizes must be responsible for the higher kinetic constant values obtained with the SBA-15 catalysts. On this basis, a particle size range around 6–7 nm appears to be the optimum value for the cyanide photooxidation with the catalysts developed in this work. The advantage of lesser scattering effects found upon increasing titania content in the $TiO_2$_commercial samples should be partially counteracted by the simultaneous increasing mean particle sizes.

## 4. Conclusions

Nanocrystalline titanium dioxide materials have been synthesised supporting the semiconductor on different mesoporous silica supports. The dispersion effect promoted by the support prevents in all cases the anatase to rutile phase transformation observed in bare $TiO_2$ materials upon identical calcination treatments. The synthesised samples have shown their activity as photocatalysts for cyanide oxidation. The use of mesostructured SBA-15 silica with proper pore diameter allows controlling the size of the obtained titania particles within the 6–7 nm range. The observed correlation between the mean pore width of this silica support and the size of the obtained titania particles is specially remarkable for materials containing up to 60 wt.% $TiO_2$ content. The mean titania particle size plays an important role in the photoactivity shown by the materials prepared in this work.

## Acknowledgements

The authors would like to thank "Consejería de Educación, Comunidad de Madrid" for the financial support of this research through the Project 07M/0050/1998 and "Grupos Estratégicos" and Ministerio de Ciencia y Tecnología for the Project PPQ2000-1287.

## References

[1] M. Schiavello (Ed.), Photocatalysis and Environment: Trends and Applications, Kluwer Academic Publishers, Dordrecht, 1988.
[2] N. Serpone, E. Pelizzetti (Eds.), Photocatalysis: Fundamentals and Applications, Wiley, New York, 1989.
[3] G. Lassaletta, A. Fernández, J.P. Espinós, A.R. González-Elipe, J. Phys. Chem. 99 (1995) 1484.
[4] Z. Ding, X. Hu, G.Q. Lu, P.L. Yue, P.F. Greenfield, Langmuir 16 (2000) 6216.
[5] N. Serpone, D. Lawless, R. Khairtudinov, E. Pelizzetti, J. Phys. Chem. 99 (1995) 16655.
[6] Y.X. Langford, C.H. Langford, J. Phys. Chem. B 101 (1997) 3115.
[7] B.J. Aronson, C.F. Blanford, A. Stein, Chem. Mater. 9 (1997) 2842.
[8] Z. Zhang, C.C. Wang, R. Zakaria, J.Y. Ying, J. Phys. Chem. B 102 (1998) 10871.
[9] C.T. Kresge, M.E. Leonowicz, W.J. Roth, J.C. Vartuli, J.S. Beck, Nature 359 (1992) 710.
[10] J. Aguado, D.P. Serrano, J.M. Escola, Micropor. Mesopor. Mater. 34 (2000) 43.
[11] D. Zhao, J. Feng, Q. Huo, N. Melosh, G.H. Fredrickson, B.F. Chmelka, G.D. Stucky, Science 279 (1998) 548.
[12] L.S. Clesceri, A.E. Greenberg, A.D. Eaton (Eds.), Standard Methods for the Examination of Water and Wastewater, 20th Edition, American Public Health Association/American Water Works Association/Water Environment Federation, MD, 1998.
[13] C.-C. Wang, J.Y. Ying, Chem. Mater. 11 (1999) 3113.
[14] M. Schiavello (Ed.), Heterogeneous Photocatalysis, Wiley, Chichester, 1997.
[15] Y. Wang, A. Suna, W. Mahler, R. Kasowski, J. Chem. Phys. 87 (1987) 7315–7322.
[16] J.J. Kuskinski, L.A. Gómez-Jahn, K.J. Faran, S.M. Gracewski, R.J. Miller, J. Dwayne, J. Chem. Phys. 90 (1989) 1253.
[17] B.V. Mihaylov, J.L. Hendrix, J.H. Nelson, J. Photochem. Photobiol. A: Chem. 72 (1993) 173.
[18] S.N. Frank, A.J. Bard, J. Am. Chem. Soc. 99 (1977) 303.
[19] V. Augugliaro, V. Loddo, G. Marcì, L. Palmisano, M.J. López-Muñoz, J. Catal. 166 (1997) 272.
[20] M. Kruk, M. Jaroniec, C.H. Ko, R. Ryoo, Chem. Mater. 12 (2000) 1961.
[21] M. Anpo, T. Shima, S. Kodama, Y. Kubokawa, J. Phys. Chem. 91 (1987) 4305.